# Solid-State Pulsed Time-of-Flight 3-D Range Imaging Using CMOS SPAD Focal Plane Array Receiver and Block-Based Illumination Techniques

Juha Kostamovaara [ID], *Senior Member, IEEE*, Sahba Jahromi [ID], Lauri Hallman [ID], Guoyong Duan [ID], Jussi-Pekka Jansson [ID], and Pekka Keränen

*Abstract*—Full realization of a solid-state 3-D range imager based on the pulsed time-of-flight method is presented. The system uses block-based segmented illumination in the transmitter realized with a 16-element common anode laser diode bar. The receiver is based on a single chip 2-D SPAD/TDC 0.35 $\mu$m CMOS array with 32 $\times$ 128 SPAD pixels and 257 TDCs. Segmentation of the illumination improves the $SN_{BG}R$ in the detection and results in simpler receiver realization than in the commonly used flood-illumination approach. The system is capable of producing cm-accurate 3-D range images within a FOV of 40° $\times$ 10° up to a range of 15 m in normal office lighting at a frame rate of $\sim$30 fps using a low average illumination power of only 2.6 mW. In background illumination of $\sim$20 klux, 3-D range images were captured at a distance of $\sim$13 m using the gated SPAD approach at a frame rate of $\sim$1 fps.

*Index Terms*—Laser radar, lidar, range imaging, single photon detection.

## I. INTRODUCTION

THREE-dimensional range imaging techniques have found applications in surveying, civil engineering (e.g., construction site mapping), inspection and quality control, for example, and recently also in autonomous vehicles [1], [2]. These applications are dominated by lidar systems that use mechanically steered light to obtain the 3-D range image, with drawbacks arising from relatively high costs and mechanical fragility [3], [4]. It is generally recognized that 3-D range imaging could well be used in many other applications such as robotics, small vehicle guidance, (e.g., unmanned aerial vehicles, UAVs), virtual/augmented reality (VR/AR), consumer electronics (games) and machine control (e.g., construction and forestry machines) [5]. Solid-state 3-D range imager realizations, i.e., systems without any mechanically moving parts, are appealing techniques for these potential new applications since they would pave the way for low costs and miniature size realization.

One successful approach to solid-state 3-D range imaging (e.g., in gesture control and games) uses a continuous wave (CW)

modulated laser beam and deduces the distance information from the phase difference between the emitted and received signal with a CMOS active pixel sensor [6]–[8]. This technology gives a high image pixel resolution, but at the cost of a limited measurement range (typically only a few meters) and a relatively high average optical illumination power (up to hundreds of milliwatts) [8]. By using several simultaneous modulation frequencies it is possible to achieve longer unambiguous measurement range without compromising the precision, but the high optical average illumination power needed remains still as an issue [9]. Optical phased arrays are interesting candidates for 3-D range imaging, but these techniques are still in an early development phase [10], [11].

Another potential solid-state technique for 3-D range imaging uses a 2-D CMOS single photon detector (SPAD) array to measure directly the round-trip transit times of the photons from the transmitter to the target and back to the receiver [12], [13]. Typical realizations following this approach use the pulsed time-of-flight (TOF) principle in which the laser diode transmitter sends pulses of length 1…10 ns to the target in the flood illumination configuration, i.e., the whole system field of view (FOV) is illuminated for each transmitted pulse [14]–[19]. A 2-D CMOS SPAD array is then positioned at the focal plane of the receiver optics. Thus, this approach resembles the focal plane array (FPA) techniques well known from CMOS image sensors. The advantages of the SPAD approach are the high sensitivity and low timing jitter inherent in single photon detection techniques. The typical sensitivity and jitter of a CMOS SPAD at NIR wavelength region are $\sim$1…5% and $<$100 ps, respectively [20]–[22]. Since the avalanche breakdown of a SPAD element can easily produce a signal in the volt range, no analogue amplifiers are needed which markedly simplifies the receiver and also eliminates the electrical cross-talk. SPADs can be realized in standard CMOS, and thus other electronics such as the time-to-digital converters that record the photon flight time intervals can also be located on the same die, which is an important advantage from the system integration point of view.

The focus of research in the latter field has up to now been mostly on the design of versatile receivers realizing a high density 2-D CMOS SPAD array and the related signal processing electronics. Most of the designs assume a flood illumination strategy, and the basic on-chip functionalities typically include

a 2-D array of SPADs (e.g., $128 \times 128$ elements), time-to-digital converters (TDC) and some histogram processing to relieve the I/O data rate load [18]. To improve the SPAD performance (e.g., fill factor, photon detection probability) separate chips may also be used for the SPAD array and the other electronics [15]. Radiometric analysis and practical demonstrations show however, that at longer distances ($>5\ldots10$ m) and with the laser pulse energies readily available from semiconductor laser diodes ($\sim10$ nJ), the per pixel photon detection probability in this kind of a measurement system, especially at the limit of the measurement range, is rather low, e.g., around 1% or even lower [16], [23]. Thus, most of the detectors are idle as far as signal detection is concerned.

Another illumination strategy tries to overcome this issue and achieve a more efficient use of the available average illumination power by illuminating the system FOV in blocks. In this strategy, the FOV is segmented into to 16 blocks, for example, and each of these is illuminated by a certain number of successive laser pulses (e.g., 5000) so that the required signal-to-noise ratio (SNR) for a successful detection of the target pixels within the illuminated segment is achieved. As described in greater details in Section II, this approach enables one to achieve a higher ratio between the number of signal photons detected and the background photons in a given time frame and with a given average illumination power (with certain assumptions concerning the measurement situation) than what is available with flood illumination [24], [25]. The practical realization of the illuminator can consist of a number of laser diode emitters which are located so that each one produces the illumination for a particular segment in the system FOV [26]. Thus, this system, which resembles mechanical scanning of the laser beam over the system FOV, can be realized in full solid state, which is an important advantage. Also, the synchronization issue known to exist when using a mechanical scanner and a SPAD-based receiver is not experienced here due to the unambiguous knowledge of which of the laser emitters is being driven at any particular time [27]. Interestingly, a similar illumination concept realized with an on-chip thermo-optic switching tree and a focal plane grating-based transmit array was recently applied to FMCW lidar based 3-D ranging with promising results [28].

We present here a full realization of a pulsed time-of-flight 3-D range imager which is based on segmented block-based illumination transmitter realized in solid-state and CMOS 2-D SPAD/TDC receiver techniques. The design principles are presented in Section II. Section III describes the realizations of the transmitter and receiver, measurements demonstrating the performance of the resulting 3-D range imager are given in Section IV, and finally, the results are discussed and compared with those of other relevant studies in Section V.

## II. MEASUREMENT CONCEPT AND DESIGN CONSIDERATIONS

The concept behind the 3-D range imager developed here is shown in Fig. 1. The transmitter consists of a custom-designed common anode laser diode bar with 16 separately addressable laser diode elements. This laser diode bar is located at the focal plane of the transmitter optics with the result that when one of
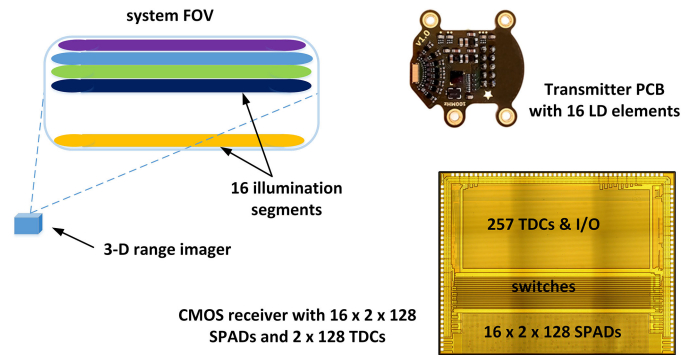


Fig. 1. Block-based illumination: concept, transmitter PCB and CMOS receiver IC.

the laser diode elements is being driven, only the corresponding segment within the field of view of the system is illuminated. On the receiver side, a custom-designed CMOS SPAD IC receiver with $32 \times 128$ SPAD elements is located at the focal plane of the receiver optics. Each of the SPAD elements in the array sees photons from a certain direction only and by measuring the transit time of these photons the 3-D range coordinates (x, y, z) of the corresponding target point can be determined. The x and y coordinates are determined by the position of the SPAD element under consideration and the z coordinate can be calculated from the measured transit time. In addition to the SPAD array, the receiver IC also contains $2 \times 128$ time-to-digital converters which can be electrically connected to any two 128-element SPAD lines within the receiver array (corresponding to the segment under illumination). Thus, the total number of TDCs needed in this realization is determined by the number of SPAD elements within a single illumination block (i.e., $2 \times 128$ in this case), and not by the total number of SPAD elements in the receiver ($32 \times 128$ in this particular design) as would be needed in a flood illumination-based system. This is an important advantage since the design of accurate TDCs typically requires a considerable circuit area.

The signal-to-noise ratio in a typical worst case measurement scenario will be discussed next. It is assumed that for a single emitted laser pulse the probability of photon detection is $<<1$ (the probability that a particular SPAD is triggered by a signal photon), which is the case in a typical measurement situation especially at the maximum end of the measurement range [23], [25]. It will be seen in the experimental section that for this particular design the signal photon detection probability at the limit of the measurement range is $\sim0.05$, which would justify the above assumption even if a markedly higher pulse energy were used. This allows one to deduce that for a valid signal detection a bunch of laser pulses (e.g., 5000) would need to be sent, and that the echo pulse detection probability would then improve proportionally to the number of laser pulses emitted.

Any noise in the measurement, especially in the potential outdoor applications suggested above, would typically come from random detections induced by the background radiation, i.e., from the sun. The intensity of the background radiation can be usefully characterized by the mean time interval between

the random detections in a SPAD, $\tau_{BG}$, a parameter which depends on the intensity of the background radiation and on certain system-level parameters that will be described in more details below. The value of $\tau_{BG}$ is typically from a few ns up to hundreds of nanoseconds, which is markedly shorter than the typical random detection rate due to SPAD internal random thermal noise (dark counts), and thus the dark counts of the detector can be disregarded.

In a typical measurement sequence a bunch of laser pulses is sent into the illuminated segment and the corresponding time histograms of detections per SPAD corresponding to the illuminated segment are collected. The illumination is then switched to the next segment by driving the next laser diode in the bar, and this procedure is then repeated for all the laser diode elements. As an example, if 5000 laser pulses were sent per segment, and the system FOV were divided into 16 segments, the frame rate with a laser driver pulsing rate of 250 kHz would be $\sim$3 fps. The per-pixel histogram would then consist of random detections due to the background noise, together with the signal hits at the time position corresponding to the transit time of the pulse to the target and back to the receiver. Matched filtering is typically used to maximize the signal-to-noise ratio during detection.

In order to be able to detect the signal echo reliably from among the background hits, the SNR should be high enough. In the following analysis, the signal-to-background noise ratio ($SN_{BG}R$) will be calculated (instead of SNR) since it clearly shows the effect of the shortening of the laser pulse (while maintaining the total pulse energy at same level) on the signal detection performance, especially on the false alarm rate. For a precise analysis of the false alarm rate and detection probabilities, complete photon statistics and multiple pulse probabilities should be used, see for example [29]–[31].

A rough estimate of the $SN_{BG}R$ can be given as the ratio between the average number of signal detections and the square root of the number of random noise detections during the laser pulse envelope, see (1). For simplicity, homogenous illumination is assumed, and the cosine effects of the optics are neglected. The number of signal photon detections can be evaluated using the well-known inverse-of-distance-squared dependent radar equation and system parameters. If we assume that the hit histogram is filtered with a simple integrator with an integration time corresponding to the width of the laser pulse ($\Delta t_{pulse}$, FWHM), the probability of detecting a noise count within the pulse envelope will be roughly $\Delta t_{pulse}/\tau_{BG}$. In (1), $E_{opt}$ is the energy of the laser pulse, $\varepsilon$ the efficiency of the optics, $\rho$ the reflection coefficient of the target, $A_{rec}$ the aperture area of the receiver optics, r the distance to the target, $E_{ph}$ the photon energy, PDP and FF are the detection efficiency and fill factor of the SPAD pixel, respectively, x and y are the total number of SPAD elements in two orthogonal directions over the receiver surface, M is the number of illumination blocks, $f_{LD}$ is the pulsing frequency of the laser transmitter, $P_{av}$ is the average illumination power and $f_{frame}$ is the desired 3-D range image frame rate. Thus, $f_{LD}/(M * f_{frame})$ is the number of laser pulses emitted for any of the target points to achieve a valid image result, and the total number of signal and background detections is proportional to this.

Since the SPADs in the receiver IC can be triggered only once per emitted laser pulse, the detection of a signal or background photon (within the pulse envelope) is possible only if no background photon is detected during the photon flight time $\Delta t_{flight}$. The probability of this follows an exponential distribution (assuming Poisson statistics) and is $e^{-(\Delta t_{flight}/\tau_{BG})}$. This term produces a serious attenuation in the signal (and background) counts and may even block the receiver if the photon flight time is longer than the mean time interval between background radiation induced detections. This attenuation can be relieved, however, if the SPADs are activated only after the emission of the laser pulse, e.g., with a time delay that corresponds to a minimum target distance of $r_{gate}$. This would shorten the active time window of the SPADs correspondingly (term r-$r_{gate}$ in (1)) and thus also improve the overall performance, as will be demonstrated in Section IV.

$$SN_{BG}R\ (r) = \frac{N_{signal\_hits}\ (r)}{\sqrt{N_{BG\_hits}}}$$

$$\approx \frac{e^{-\frac{2\cdot(r-r_{gate})}{\tau_{BG}\cdot c_{light}}}\cdot\left(\frac{E_{opt}\cdot\varepsilon\cdot\rho\cdot A_{rec}}{\pi\cdot r^2\cdot E_{ph}}\cdot\frac{PDP\cdot FF}{\left(\frac{x\cdot y}{M}\right)}\cdot\frac{1}{M}\cdot\frac{f_{LD}}{f_{frame}}\right)}{\sqrt{e^{-\frac{2\cdot(r-r_{gate})}{\tau_{BG}\cdot c_{light}}}\cdot\frac{1}{M}\cdot\frac{f_{LD}}{f_{frame}}\cdot\frac{\Delta t_{pulse}}{\tau_{BG}}}}$$

$$= \sqrt{e^{-\frac{2\cdot(r-r_{gate})}{\tau_{BG}\cdot c_{light}}}}\cdot\frac{\left(\frac{E_{opt}\cdot\varepsilon\cdot\rho\cdot A_{rec}}{\pi\cdot r^2\cdot E_{ph}}\cdot\frac{PDP\cdot FF}{\left(\frac{x\cdot y}{M}\right)}\cdot\frac{1}{M}\cdot\frac{f_{LD}}{f_{frame}}\right)}{\sqrt{\frac{1}{M}\cdot\frac{f_{LD}}{f_{frame}}\cdot\frac{\Delta t_{pulse}}{\tau_{BG}}}}$$

$$\propto \frac{P_{av}}{\sqrt{f_{LD}}\cdot\sqrt{\Delta t_{pulse}}}\cdot\frac{\sqrt{M}}{\sqrt{f_{frame}}} \qquad (1)$$

Equation (1) allows one to evaluate the performance of the 3-D range imager once the system parameters are known. Of course, one needs also to ensure that the total number of detected signal photons is high enough for the required system performance. The added advantage of (1) is that it also gives a clearly visible insight into the optimization the system. It can be seen, for example, that the $SN_{BG}R$ can be improved if the pulse energy is compressed into short pulses, which in addition would improve the precision of the measurement. Also, assuming a certain available average illumination power, it would be useful to concentrate this into high energy pulses emitted at a lower rate rather than using a higher pulsing rate with a lower pulse energy. The higher the signal photon detection probability is, the lower the number of laser pulses needed for valid signal detection, whereupon the number of random noise detections will also be lower.

It is also evident that the use of segmentation will improve the performance. The reason for this is that for the same average illumination power, segmentation will give an M times higher irradiance on the target segment and thus also an M times higher photon detection probability in the receiver. This will result in an improved $SN_{BG}R$ since the number of noise counts will be reduced by M (M times less laser pulses are needed). The improved $SN_{BG}R$ can be used to increase the measurement range or maximum range.

The use of segmentation would also reduce the number of TDCs needed in the receiver relative to a flood illumination-based system (by a factor of 16 in the above example), which would markedly reduce the receiver complexity. Due to the electric control maintained over the segments, the illumination can be adaptive in the sense that the illumination sequence can be selected freely depending on the needs of the application and also changed during operation (e.g., the system FOV can be traded off against faster measurement or a longer range).

Another interesting design consideration can be discovered by looking in more detail at how the mean time interval between background illumination -induced detections, $\tau_{BG}$, depends on the level of background radiation and the target and system parameters. The time interval $\tau_{BG}$ can be calculated based on the background illumination power $P_B$ as seen from the active area of the SPAD element, the photon energy $E_{ph}$ (e.g., $2.5 \cdot 10^{-19}$ J at $\sim$810 nm), and the probability of a photon detection, PDP, in the SPAD ($\sim$4% at 810 nm in CMOS) as given in (2)–(4).

$$\tau_{BG} = \frac{1}{PDP}\left(\frac{E_{ph}}{P_B}\right) \tag{2}$$

$$FOV_{SPAD} = \frac{\Phi_{SPAD}}{f_{rec}} \tag{3}$$

$$P_B \approx I_S \cdot A_{rec} \cdot \rho \cdot \left(\frac{FOV_{SPAD} \cdot \sqrt{FF}}{2}\right)^2 \cdot BW_{opt} \tag{4}$$

In (2)–(4), $I_S$ is the spectral irradiance of the background radiation on the target surface at $\sim$810 nm (maximum $\sim$700 mW/(m²∗nm), corresponding to $\sim$100 klux), $A_{rec}$ is the area of the receiver aperture, $\Phi_{SPAD}$ the diameter of the SPAD element, $f_{rec}$ the effective focal length of the receiver optics, $\rho$ (e.g., $0.5/\pi$ sr$^{-1}$) the reflection coefficient of the Lambertian target, $BW_{opt}$ the optical bandwidth of the receiver (e.g., 50 nm) and FF the fill factor of the SPAD detector element. $FOV_{SPAD}$ is the linear field of view of a single SPAD element given in radians. As can be seen, $P_B$ does not depend on distance, but is strongly dependent on the FOV of the SPAD. To reduce the background power, narrow optical filtering is preferred, but the passband of the spectral filter must be wide enough to accommodate wavelength shifts caused by variations in temperature and the angle of incidence of the optical rays.

Interestingly, we now see from (1) that in this kind of system (one detection per laser shot), there is an optimum size for the receiver aperture [29], [30], [24]. While an increase in the receiver aperture would in principle improve the $SN_{BG}R$ (proportional to $\sqrt{A_{rec}}$), the exponential attenuation effect would increase as well, due to the inverse dependence of the $\tau_{BG}$ on the aperture size. At large aperture size the latter effect will dominate and thus there is typically an optimum aperture size to be found under high background illumination conditions which will maximize the measurement range. Optimization can also be achieved, of course, by means of a variable optical attenuator in front of the receiver, or by changing the PDP of the SPAD, for example.
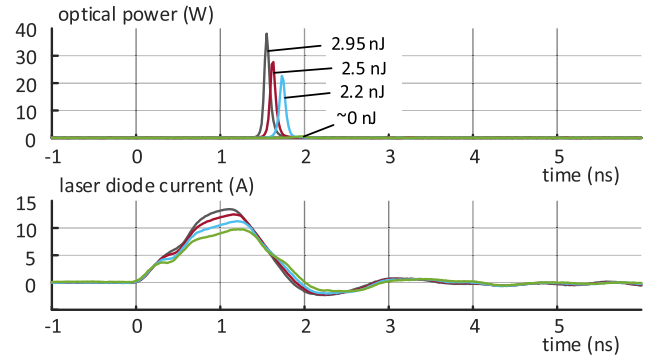


Fig. 2. Optical output power and corresponding drive current pulse shapes for a single laser diode element in the 16-element common anode laser diode bar, gate pulse width $\sim$1 ns.

## III. SYSTEM DESIGN

### A. Block-Based Illuminator

The emitter of the transmitter is a custom designed laser diode (LD) bar with 16 individual emitting elements. The laser diodes have a common anode contact and separate cathode contacts allowing n-type driver transistors and thereby simplifying the transmitter design. The pitch of the laser diode bar is 300 µm. The individual elements have an active layer stripe width and cavity length of 150 µm and 1.5 mm, respectively. The wavelength of the laser radiation is $\sim$810 nm. The active layer of each laser consists of five GaAs/AlGaAs quantum wells each 40 Å thick, and thus the total thickness of the active material is $d_a \sim$200 Å. The active layer is positioned towards the p-cladding so that the equivalent spot size $d_a/\Gamma$ (where $\Gamma$ is the optical confinement factor), is relatively large ($> \sim$3 µm). As shown in our earlier work, a high value for the equivalent spot size will enable the accumulation of a large number of carriers in the active layer before the emission of the gain-switching pulse, leading to high gain-switching pulse energy (enhanced gain switching) [32], [33]. This kind of design allows for the generation of sub-ns optical pulses of relatively high energy (nJ regime) even when driven with markedly longer current pulses (ns range) [34]. As an example of this, Fig. 2 shows the optical output of one laser diode element in the bar when driven with current pulses of different amplitudes and a length of $\sim$1 ns (FWHM) at 1 kHz. As can be seen, the maximum drive current of $\sim$13 A results in a single isolated optical pulse with a length of $\sim$100 ps and peak power of $\sim$35 W. Thus, the pulse energy is $\sim$3 nJ which is considerably more than that achieved from gain-switched laser diodes with a conventional structure [35], [36]. It is also seen that as a result of the design, the threshold current of such a structure is relatively high, i.e., $\sim$10 A in this case. For this reason, there is no optical output for the laser with the lowest drive current pulse (peak current <10 A).

Fig. 3 shows a schematic diagram of the laser transmitter electronics. An FPGA controller triggers the GaN drivers sequentially with a pulsing rate of 256 kHz, providing pulses of adjustable widths to the gates of the GaN switches, so that the pulsing rate of each of the laser diodes is 16 kHz (256 kHz/16). Of course, other type of pulse sequences can also be realized
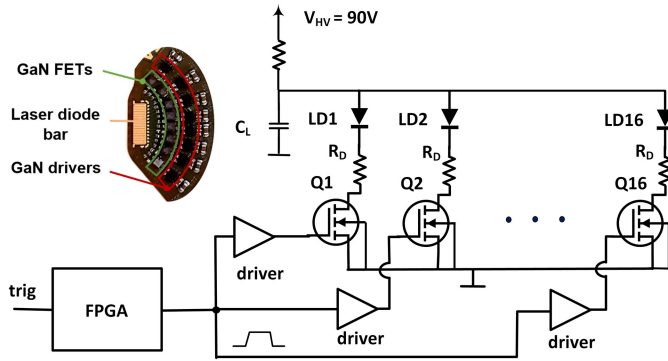
Fig. 3. Schematic diagram of the 16-element laser diode bar driver electronics and details of the printed circuit board realization of the 16-element block-based illuminator.
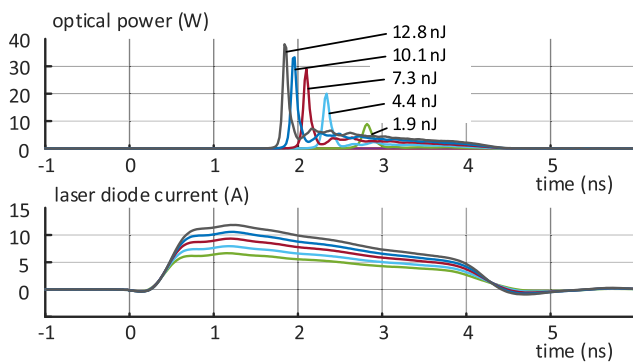


Fig. 4. Optical output power and corresponding drive current pulse shapes for a single laser diode element in the 16-element common anode laser diode bar, gate pulse width $\sim$3.5 ns.



Fig. 5. Photograph of the time-averaged illumination pattern of the transmitter measured at a distance of $\sim$1 m.



Fig. 6. Micro-photograph of the receiver IC showing the $32 \times 128$ SPAD array, the 257 element TDC array and the switches controlling the active receiver block with $2 \times 128$ SPAD and 256 TDC elements.

easily, just by changing the code of the FPGA. The PCB realization of the driver part of the transmitter is also shown in Fig. 3. The total anode capacitance is estimated to be $\sim$700 pF (including the anode stray capacitance in the laser diode bar), and the series resistor $R_D$ was varied between 2.5 $\Omega$ (the result of Fig. 2) and 5 $\Omega$ (the result of Fig. 4).

In the system test the laser diodes were driven with longer $\sim$3.5 ns current pulses to increase the energy of the resulting optical pulses. Fig. 4 shows the resulting driver current and optical pulses within the HV supply range of 50 to 90 V for a single laser diode element in the bar. The optical pulses now show a tail of length $\sim$2 ns, which increases the total maximum pulse energy to $\sim$10 nJ. The total power consumption of the transmitter with a driver pulsing rate of 256 kHz is $\sim$1 W. It should also be noted that for ns-range optical pulses a conventional double heterostructure laser diode structure (optimizing optical confinement) can well be used in the transmitter.

Cylindrical optics are used to shape the optical radiation of the laser diode bar into a system illumination cone of $40° \times 10°$ (FWHM). When focused to infinity, 16 illumination segments with a separation corresponding to the height of the segment are formed (see Fig. 5 for the measured time-averaged illumination pattern). As explained above, in reality only one of the 16 segments is illuminated at a time. The illumination pattern can
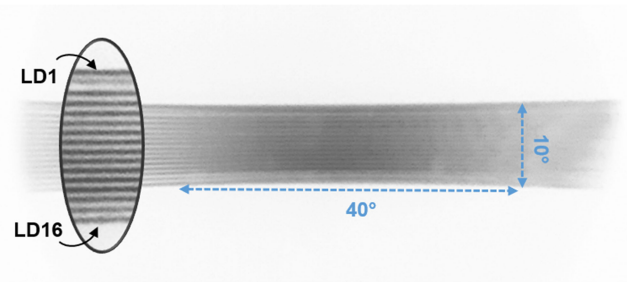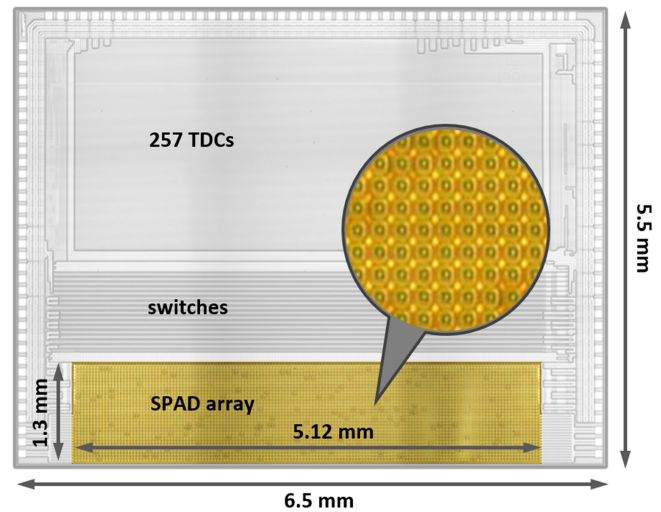
be made to be more homogenous by slightly misfocusing the transmitter [26].

### B. Receiver

The custom-designed receiver is a 6.6 mm $\times$ 5.5 mm integrated circuit (IC) consisting of a $128 \times 32$ SPAD array and a 257-channel TDC array, realized in 0.35 $\mu$m HV CMOS technology. A micrograph of the IC is shown in Fig. 6. The light-sensitive part of the IC, which has a fill-factor of $\sim$35%, is highlighted. The inset in Fig. 6 shows a zoomed version of the SPAD array with each SPAD having a 40 $\mu$m $\times$ 40 $\mu$m pitch (active area of 26 $\mu$m $\times$ 21 $\mu$m) and a deep-nwell cathode/p+ anode junctions (a shared cathode structure).

A block diagram of the receiver as part of the 3-D imager system is shown in Fig. 7. The SPAD array can be regarded as 16 blocks, each consisting of two adjacent rows ($2 \times 128$ SPADs), and any of these blocks can be connected to the 256 TDC bank in each measurement through tri-state buffers. The 257th TDC is always reserved for measuring the start transmission of the laser pulse. The TDCs can measure with a resolution of $\sim$78 ps.

The operation time of the SPADs can be limited during each measurement (gated mode) to suppress dark and background light-induced detections from blocking the SPADs before the
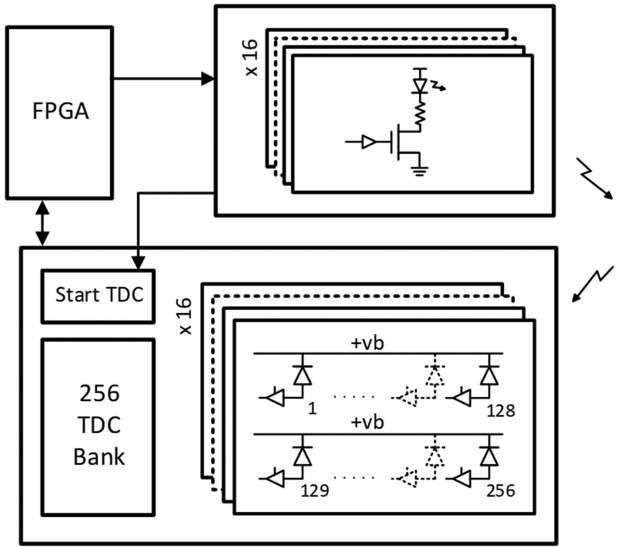
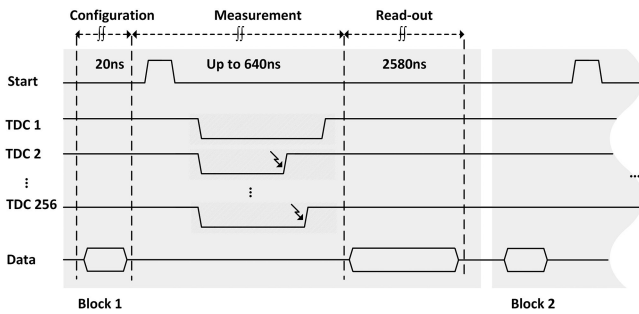Fig. 7.    Block diagram of the receiver IC as part of the 3-D imager.



Fig. 8.    Timing diagram of receiver operation during the imaging of one block.



Fig. 9.    Photograph of the target scene in indoors measurements.
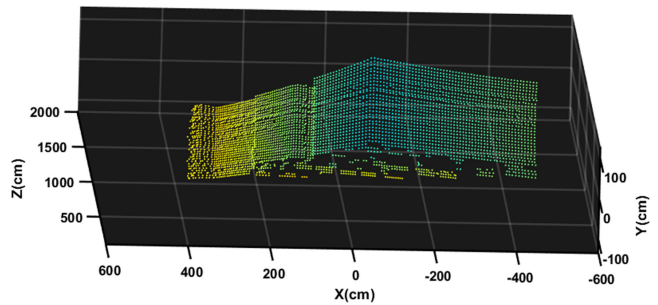


Fig. 10.    3-D range image of the scene shown in Fig. 9 measured with 8192 laser shots per pixel, equivalent frame rate ∼2 fps.

arrival of the laser pulse photons. The width and delay of the gate windows can be adjusted between 5 ns and 635 ns (with 5 ns resolution) depending on the measurement conditions.

Matching scans of the LD array and the SPAD array can be performed in 16 cycles for the 16 blocks (in a block-based illumination scheme) to cover the whole field of view. A timing diagram of receiver's operation during one cycle for one block is shown in Fig. 8. At the beginning of each cycle, the IC is configured for the measurement (i.e., a block is chosen for the measurement and the gate window is set), then the time of the start signal and SPAD detections are measured by the respective TDCs, and finally the measured data are read out from the IC. The cycle for one block can be repeated the desired number of times before moving on to the next block. More details of the design and performance of the receiver circuit are presented in [25].

## IV. 3-D RANGE IMAGE DEMONSTRATIONS

### A. Indoor Measurements

Since the basic properties of the SPAD based pulsed time-of-flight imaging, e.g., its precision and the dependence of this on pulse length and the averaging of successive results, have been well covered in prior research, see [37], [38], [23] and references therein, the emphasis in the experimental section of the current study will be on demonstrating the functionality of a 3-D range imager in various measurement situations. In fact, in spite of quite active research in this field, there have been so far only a few full solid-state realizations (including transmitter and receiver) to demonstrate the recording of 3-D range images, especially under high background illumination conditions [16], [17], [25], [39].

In order to demonstrate the functionality of the 3-D range imager developed here, system test measurements were carried out both indoors and outdoors. The aperture and focal length of the receiver optics were 5.6 mm and 6.7 mm, respectively, and an optical bandpass filter bandwidth of 40 nm (FWHM) was used to reduce the effect of the background illumination. The field of view (FOV) of the receiver was ∼40° × 10°.

A picture of the target scene for the indoors measurements (a classroom) is shown in Fig. 9, and the corresponding 3-D range image (point cloud) recorded at a frame rate of ∼2 fps is shown in Fig. 10.

The laser drive rate was 256 kHz, and the radiation from a single laser diode element fell on two lines of SPAD elements at a time. 8192 laser shots were recorded per pixel so that the equivalent frame rate with 16 laser diode elements was ∼2 fps. The average laser power used for illumination was ∼2.6 mW. The signal processing of the hit histograms of the 32 × 128
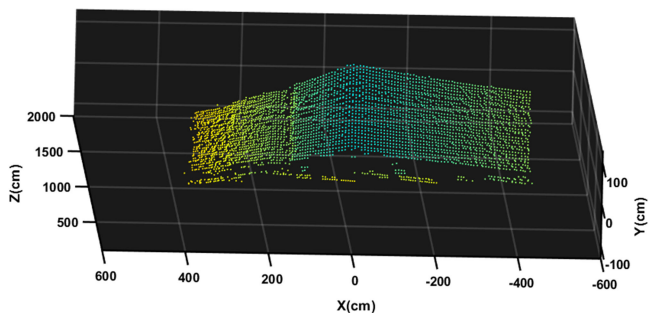
Fig. 11. 3-D range image of the scene shown in Fig. 9 measured with 512 laser shots per pixel, eq. frame rate ∼30 fps.
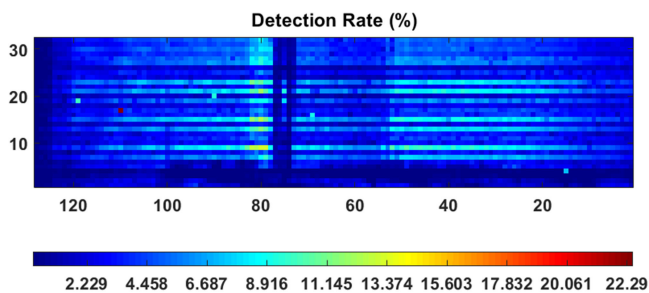


Fig. 12. Detection rate over the 2-D SPAD array with 32 × 128 pixels in the measurement situation represented in Fig. 10.
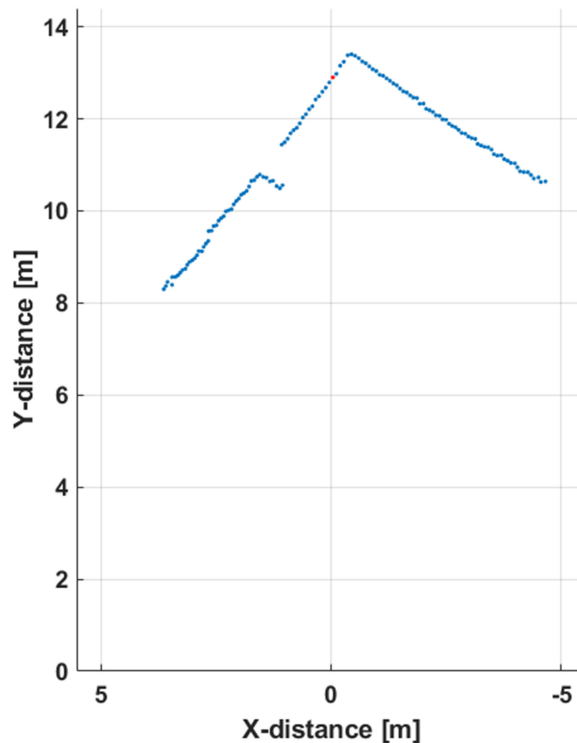


Fig. 13. Line profile of the row 15 in the point cloud of 32 × 128 pixels measured with 512 laser shots in the measurement situation of Figs. 9 and 11.
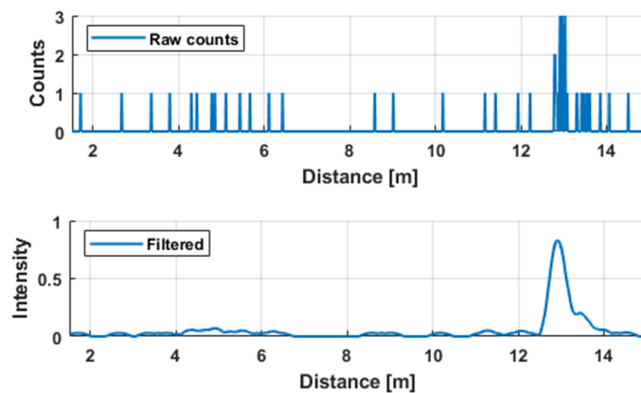


Fig. 14. Raw count (upper curve) and filtered intensity histograms (lower curve) for one of the points in the result depicted in Fig. 13(marked with a red dot in Fig. 13).

points included calibration of the static on-chip delay differences within the receiver IC and of the distortion of the receiver optics. The raw histogram was filtered using the shape of the optical laser pulse as the filtering time-domain template (i.e., matched filtering). The distance result was determined by finding the channel with maximum number of detections and then averaging the result around it.

Most of the target points were located on the walls at the back and to the left of the scene, while some detector elements were hit from the tables as well. The distance to the back wall was ∼13…15 m. It is seen that the target shapes in the scene are quite well recorded under normal office lighting. The shape of the black pole to the left of the scene, for example, is clearly seen in the recorded 32 × 128 pixel 3-D range image.

For comparison, Fig. 11 shows the same scene measured with 512 laser shots per point, in which case the equivalent frame rate is ∼30 fps. Some point results are now missing, e.g., from the surface of the black pole on the left of the image. The point cloud quality is still relatively good, however.

The detection rates of pixels in the 32 × 128 SPAD array during the measurement shown in Fig. 10, i.e., with the rate of ∼2 fps, as shown in Fig. 12, are seen to vary in the range 1…10% over the image area. The lower detection probability at the sides of the pole is clearly visible in the detection rate map (columns 75…80), and it is evident that one of the laser diodes in the bar is emitting considerably lower power than the others (rows 3-4). The lower intensity in every other row is due to the gap between the laser diode emitters (150 $\mu$m).

The line profile of one of the 32 rows, in this case row no. 15, as measured in the situation shown in Fig. 11 using 512 laser shots

per point, is shown in Fig. 13. For this purpose a simple parabolic filter with a FWHM width approximately fitted to the laser pulse width was used to filter the raw histogram data. The profiles of the wall on the left side of the figure are well recognizable. It is also seen that the variation in the results, e.g., on the back wall increases towards the right side of the picture, which is due to the lower numbers of detections in that region.

As an example of the measured histograms, Fig. 14 shows the raw and filtered data of one of the points from the 32 × 128 point cloud. The data shown were recorded from the point marked with a red dot in Fig. 13. The upper curve in Fig. 14 shows the raw data and the lower curve the filtered histogram. The time histogram consists of the random hits caused by the background
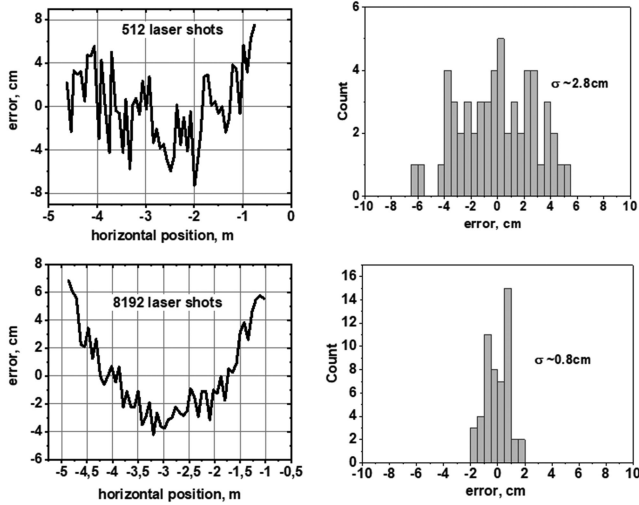
Fig. 15.    Point-wise error and their distributions for the line profile shown in Fig. 13 for the part of the back wall on the right side of the corner. The upper boxes are for 512 laser shots and the lower ones for 8192 laser shots.



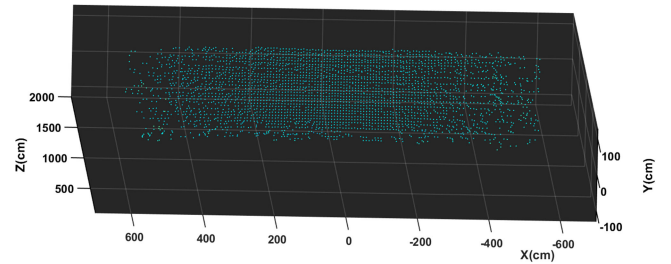Fig. 16.    Photograph of the target scene in the outdoors measurements.



Fig. 17.    3-D range image from the scene at a distance of ~13 m (Fig. 16) measured with 16 000 laser shots per pixel, eq. frame rate 1 fps with gating of the SPADs 5 m before the target surface. Background illumination level ~20 klux.

radiation and the signal hits within the pulse envelope of 0.3 m (corresponding to the pulse length ~2 ns) at a distance of 13 m. The number of hits within the pulse envelope in this particular point was 29 (out of 512 laser pulses emitted), which conforms to expectations in the light of (1) (within the limits of the statistics and the uncertainty with regard to some parameters). Due to the low background illumination (office lighting), the SNR in the measurement is defined solely by the signal photon statistics.

In order to appreciate the available precision, the error distributions for the points along the back wall (right-hand part of the line profile) in Fig. 13 were analyzed for 512 and 8192 laser shots, respectively. The error distributions are shown in Fig. 15. The upper boxes show the point-wise error for 512 laser shots and the lower boxes that for 8192 laser shots. As is seen, more clearly from the results with 8192 laser shots due to the higher averaging, the calibration of the distortion of the receiver optics was not entirely accurate since it shows a quadratic dependence on the horizontal measurement position. This error was then removed in order to focus more clearly on the random error, which was markedly smaller for the higher number of laser pulses. Given an average detection rate over the whole line of ~5%, the expected precision for 512 laser shots would be $\Delta t_{\text{pulse}}$/SQRT($0.05 \times 512$) ~ 2000 ps/5 = 400 ps (FWHM) in time. Assuming a relation of $\sigma$ = FWHM/2.35 (accurate for a Gaussian pulse), a sigma value of 170 ps is achieved for the precision. This corresponds to a distance precision of 2.55 cm (170 ps/67 ps) which is quite close to the measured precision of 2.8 cm shown in Fig. 15. For 8192 laser shots the precision should be 4 times better, i.e., 100 ps/1.5 cm (FWHM) in time/distance, which improvement is also seen in the result of Fig. 15.

## B.  Outdoor Measurements

In order to demonstrate the effect of gating on the quality of the 3-D range images, some outdoor tests were also performed,

the test environment for which is shown in Fig. 16. The weather during the measurements was windy with 50% cloud cover. The background illumination level measured at the surface of the target wall (gray concrete) varied between 10 klux and 60 klux.

In the first measurement the distance to the wall was ~13 m. As explained in Section III-B, the SPADs of the receiver array can be activated at any time after the laser pulse with a resolution of 5 ns. This technique reduces the exponential attenuation, thus improving the measurement performance. In the measurement situation shown in Fig. 16, for example, with ~20 klux background illumination, 3-D range imaging was not successful without gating. When the SPADs were activated about 5 m before the target location, however, the measurement was already operative for most of the image points, especially at the center of the image area. The measured point cloud is shown in Fig. 17. In this measurement 16 000 laser shots were used for each of the image points and thus the equivalent frame rate with a driver rate of 256 kHz was 1 fps.

The raw histogram data for a few points on row 16 are shown in Fig. 18. The exponential dependence of the background hits is clearly seen due to the relatively high background illumination level. The time constant $\tau_{\text{BG}}$ can be evaluated to be ~20 ns which corresponds to background illumination of ~20 klux in this particular measurement situation. The position of the SPAD activation is at ~8 m. In this raw data the positions of the target points at ~13 m are barely noticeable.
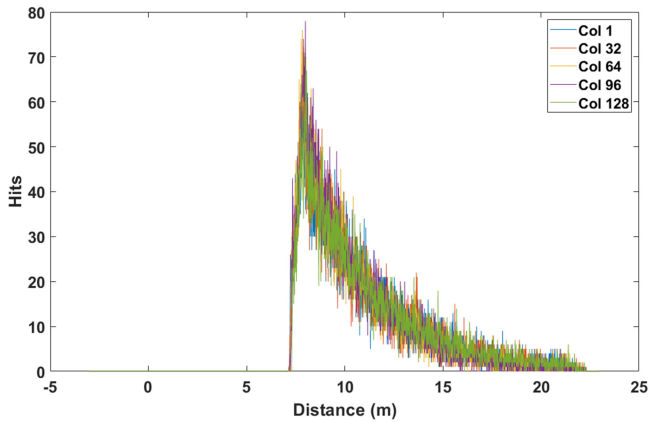
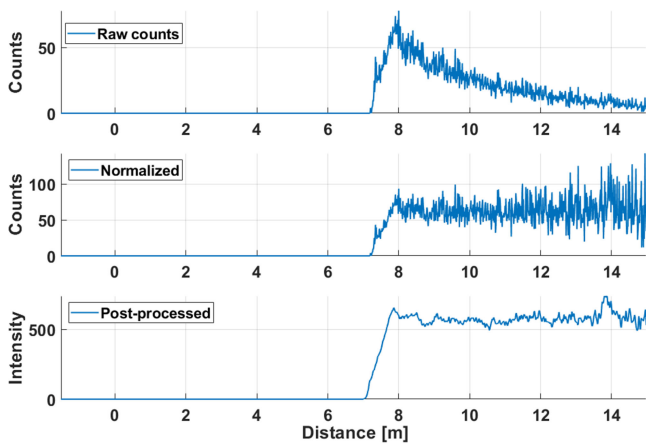Fig. 18. Raw histogram data from a few points on row 16 in the measurement situation shown in Fig. 16.



Fig. 19. Raw counts, normalized counts and post-processed intensity histogram for one of the points (row 16, column 96) in the measurement situation of Fig. 16.

For outdoor measurements the signal processing included compensation of the exponential attenuation (normalization in Fig. 19, not necessary in indoors measurements, see [40], [41], and matched filtering (presented as post-processed intensity in Fig. 19). As an example of this processing, the corresponding histograms for one of the points in the point cloud image (row 16, column 96) are shown in Fig. 19. The $SN_{BG}R$ estimated from Fig. 19 at the target distance is 5...10 which is in line with the prediction based on (1).

At a slightly lower background illumination intensity (~12 klux) and with tighter gating (~20 ns before the target surface, equivalent to 3 m), the image quality was improved, as shown in Fig. 20. It is also evident that measurement is not successful for one of the laser diode elements even in this case (rows 3 and 4).

## V. DISCUSSION AND SUMMARY

The full realization of a solid-state 3-D range imager based on the pulsed time-of-flight method has been described above. The system employs block-based segmented illumination in the transmitter and a single chip 2-D SPAD/TDC 0.35 um CMOS
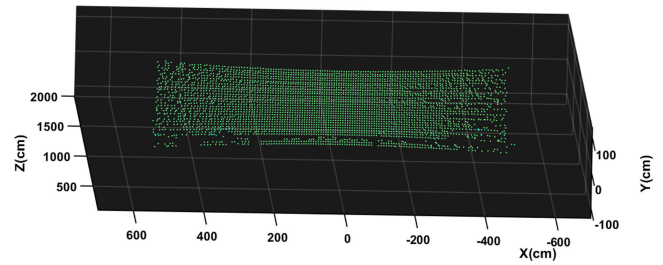


Fig. 20. 3-D range image of the scene in Fig. 16 measured with 16 000 laser shots per pixel, eq. frame rate 1 fps and with gating of the SPADs 3 m before the target surface. Background illumination level ~12 klux.

array with $32 \times 128$ SPAD pixels and 257 TDCs in the receiver. The illuminator is constructed using a custom-developed common-anode LD bar which is driven with GaN FETs working in such a way that any of them can be separately addressed. Thus, the illuminator works effectively as a solid-state scanner, i.e., scans the system FOV in blocks without any mechanically moving parts. The segmentation of the illumination results in a higher $SN_{BG}R$ -ratio in the detection and a simpler receiver realization (in terms of the number of TDCs needed) than with the typically used flood-illumination approach, assuming equal average illumination power. A photon detection probability of $<<1$ and background noise limited measurement are assumed in this comparison. Certain design consideration with regard to gating of the SPAD detectors and optimization of the receiver aperture were also discussed.

The improvement in performance is proportional to the square root of the number of blocks used. In this particular realization a custom-designed common anode laser diode bar based on QW laser diodes working in the enhanced gain switching regime was used as the laser transmitter, although when working with a ns pulse regime for a longer range, an array based on standard double heterostructure (DH) pulsed laser diodes would be a possibility, and in view of the lower threshold current, an even better choice. Another option could be a VCSEL (vertical cavity surface emitter laser) diode array with addressable sub-array blocks. This approach might allow for a large number of illumination sub-blocks and simpler realization of the transmitter optics, since the dimensions of the VCSEL array and its sub-blocks can be scaled to correspond to the desired illumination pattern. Another VCSEL transmitter approach would be to use the unit laser elements of the VCSEL array to directly define the spatial resolution of the measurement (rather than the SPAD elements of the receiver array) [42].

It was shown here that the system is capable of producing relatively accurate 3-D range image results (at the level of a few cm) with $32 \times 128$ pixels (FOV $40° \times 10°$) up to a range of 15 m in normal office lighting at a frame rate of ~30 fps using a low average illumination power of only 2.6 mW. In fact, 3-D range images were still captured at a distance of ~13 m in relatively high background illumination of ~20 klux using the gated SPAD approach, although at a lower frame rate of ~1 fps. These results compare quite well with those of a very recent state-of-the art study that demonstrates 3-D range images obtained at a frame

TABLE I
COMPARISON WITH STATE-OF-THE-ART SPAD dToF 3-D RANGE IMAGERS

| Parameters | Units | This work | OJSCC'21 [39] | JSSC'19 [43] |
|---|---|---|---|---|
| | | | | |
| Transmitter configuration | | 16-element LD bar in block-based illumination | VCSEL in flood ill. | LD-diffuser in flood ill. |
| Repetition rate | MHz | 0.25 | 10 | 40 |
| Average power | mW | 2.6 | 90 | 2 |
| Wavelength | nm | 810 | 940 | 637 |
| Receiver technology | | 0.35um CMOS | 65nm stacked CMOS | 180 nm CMOS |
| Pixel Array | | 32 x 128 | 160 x 240 | 252 x 144 |
| Pixel pitch | um | 40 | 16 | 28.5 |
| Fill factor | % | 35 | 50 | 28 |
| System FOV | deg | 40 x 10 | 63 x 41 | 40 x 20 |
| Max. distance in 3-D | m | 13/15 | 4/13.5 | 0.7* |
| Background light | klux | 20/office | 10/office | dark |
| Frame rate | frame/sec | 1/30 | 20/4 | 30 |
| Precision in 3-D | $\sigma$, cm | -/2.8 | -/0.9 | ** |
| Transmitter/receiver power consumption | W | 1/0.18 | -/0.3 | /2.5 |

*Half of the array used in 3-D, **not defined in 3-D.

rate of 4 fps at a distance of ∼13 m with a VCSEL based flood illuminator working at an average illumination power of 90 mW in a pulsed time-of-flight set up. The two-tier CMOS receiver (FOV 63° × 41°) includes 240 × 160 SPAD elements in the top tier. These are divided into sub-groups of 8 × 8 SPAD elements which all are served by a time-to-digital converter and digital processor located on the lower tier, thus the total number of on-chip TDCs (and the maximum number of detections per emitted laser pulse) is 600 [39]. The measurement distance achieved in moderately high background illumination of ∼10 klux was 4 m at a frame rate of 20 fps [39]. A more detailed comparison of this work and the study referred above and another development within this field is given in Table I.

Another interesting comparison can be made with a recent study that uses a similar illumination concept realized with an on-chip thermo-optic switching tree and a focal plane grating-based transmission array in an FMCW (frequency modulated continuous wave) lidar configuration using a narrow-band fixed-frequency 1550 nm laser in CW mode frequency modulated with a Mach-Zehnder modulator [28]. The study demonstrates distance measurement with mm-level precision in a measurement range of several tens of meters with 32 × 16 pixels, although within a small field of view of ∼2° × 2°. The added advantage of the FMCW lidar is that in addition to the target distance, its velocity can also be analyzed from the measured beat frequency. The average illumination power used was 4 mW and the (estimated) equivalent frame rate ∼9 fps. The small FOV allows for a long focal length and thus a relatively large aperture of 25 mm. It is clear from Section II that the use of a much smaller system FOV in the work described in this paper would have improved the performance considerably. Practical applications, however, typically require a FOV in the range considered here or even larger.

One obvious way to improve the performance of the technology developed, especially the maximum range in a harsh background environment, is to use short ns-scale or even sub-ns laser pulses with higher peak power and pulse energy, and to increase the number of sub-blocks in the illuminator. The limitations here arise from the challenge in constructing high speed and high current drivers, since each of the blocks should be driven with >10 A ns-range current pulses. With a standard broad-stripe DH laser diode a pulse energy of 50 …100 nJ seems feasible with 1 …2 ns pulse widths. Some improvement can be achieved by increasing the pulsing rate to the driver, however, by considering the allowed maximum average optical illumination power from the point of view of eye safety, the increase in the power consumption of the transmitter and related cooling issues, and also the increase of the I/O load of the interfaces. For example, a pulsing rate of ∼1 MHz should be possible for the transmitter used in this work without any severe cooling issues. With a VCSEL-based approach the number of illumination blocks could conveniently be higher than with separate laser diode elements or even with a laser bar structure.

From the receiver design point of view, the rate of background illumination induced random hits (and thus noise and blocking) can be effectively reduced by reducing the field of view for the SPAD unit element. This can be achieved either by increasing the focal length of the receiver optics and/or by decreasing the area of the unit element. To retain the system FOV, however, the number of pixels has to be increased, which then partly counteracts the improvement in $SN_{BG}R$. One other possible approach for overcoming this is to decouple the system and unit element FOVs by means of a segmented matrix-type transmitter. Thus, the block-based VCSEL illuminator offers an interesting approach and certainly deserves further studies.

Another option to reduce the blocking in the receiver is to construct the image pixel from several free-running SPADs (using the same equivalent pixel size), which would work independently from each other and whose results are summed up to get the macro-pixel histogram. Preliminary system level simulations show that a SPAD dead time corresponding to the level of maximum range (e.g., 100 ns in 10 m range) with 4 sub-pixels, for example, would reduce quite efficiently the blocking effect. In this approach, the use of several sub-pixels would allow the longer dead time for the SPAD, which would simplify the design of the receiver.

To conclude, the current approach seems to pave the way for the development of fully solid-state 3-D range imagers, which can be realized in relatively small size, e.g., for machine guidance and control in the construction industry, forestry and agriculture. The technology should be able to give a range of up to several tens of meters with ∼10 k spatial resolution, a relatively wide system FOV, cm-range precision (with ns-scale optical pulses) and a frame rate of 10 …30 fps under harsh background illumination conditions. Operation in bright sunlight (∼100 klux) is certainly a challenge, as for any other SPAD-based lidar approach for that matter but could at least partly be alleviated by advanced gating or freely running SPAD element approaches, for example. In general, more research in the field of advanced illumination techniques is needed, since

this topic is definitely a critical bottleneck in our research into SPAD based pulsed TOF 3-D range imaging.

## REFERENCES

[1] P. F. McManamon, *Lidar Technologies and Systems*, USA: SPIE Press, 2019, pp. 504.

[2] G. M. Williams, "Optimization of eye-safe avalanche photodiode lidar for automobile safety and autonomous navigation systems," *Opt. Eng.*, vol. 56, no. 3, Mar. 2017, Art. no. 031224.

[3] J. Kidd, "Performance evaluation of the velodyne VLP-16 system for surface feature surveying," MSc thesis, Univ. New Hampshire, 2017.

[4] B. Schwarz, "Mapping the world in 3D," *Nat. Photon.*," vol. 4, no. 7, pp. 429–430, Jul. 2010.

[5] V. C. Coffey, "Imaging in 3-D: Killer apps coming soon to a device near you!," *Opt. Photon. News*, vol. 25, no. 6, pp. 36–43, 2014.

[6] R. Lange and P. Seitz, "Solid-state time-of-flight range camera," *IEEE J. Quantum Electron.*, vol. 37, no. 3, pp. 390–397, Mar. 2001.

[7] T. Oggier *et al.*, "An all-solid-state optical range camera for 3D real-time imaging with sub-centimeter depth resolution (SwissRanger)," in *Proc. SPIE Opt. Des. Eng.*, vol. 5249, St. Etienne, France, 2004, pp. 534–545.

[8] C. S. Bamji *et al.*, "A 0.13 um CMOS system-on-chip for a 512 × 424 time-of-flight image sensor with multi-frequency photo-demodulation up to 130 MHz and 2 GS/s ADC," *IEEE J. Solid State Circuits*, vol. 50, no. 1, pp. 303–319, Nov. 2015.

[9] A. P. P. Jongenelen, D. A. Carnegie, A. D. Payne, and A. A. Dorrington, "Maximizing precision over extended unambiguous range for TOF range imaging systems," in *Proc. IEEE Instrum. Meas. Technol. Conf.*, Austin, TX, USA, 2010, pp. 1575–1580.

[10] C. V. Poulton *et al.*, "Long-range LiDAR and free-space data communication with high-performance optical phased arrays," *IEEE J. Sel. Top. Quantum Electron.*, vol. 25, no. 5, Sep./Oct. 2019, Art. no. 7700108.

[11] S. A. Miller *et al.*, "512-element actively steered silicon phased array for low-power LIDAR," in *Proc. Conf. Lasers Electro-Opt.*, San Jose, CA, USA, 2018, pp. 1–2.

[12] M. A. Albota *et al.*, "Three-dimensional imaging laser radar with a photon-counting avalanche photodiode array and microchip laser," *Appl. Opt.*, vol. 41, pp. 7671–7767, Dec. 2002.

[13] C. Niclass, A. Rochas, P. Besse, and E. Charbon, "Design and characterization of a CMOS 3-D image sensor based on single photon avalanche diodes," *IEEE J. Solid-State Circuits*, vol. 40, no. 9, pp. 1847–1854, Sep. 2005.

[14] M. Perenzoni, D. Perenzoni, and D. Stoppa, "A 64 x 64-Pixels digital silicon photomultiplier direct TOF sensor with 100-MPhotons/s/pixel background rejection and imaging/altimeter mode with 0.14% precision up to 6 km for spacecraft navigation and landing," *IEEE J. Solid-State Circuits*, vol. 52, no. 1, pp. 151–160, Jan. 2017.

[15] S. W. Hutchings *et al.*, "A reconfigurable 3-D-Stacked SPAD imager with in-pixel histogramming for flash LIDAR or high-speed time-of-flight imaging," *IEEE J. Solid-State Circuits*, vol. 54, no. 11, pp. 2947–2956, Sep. 2019.

[16] H. Ruokamo, L. W. Hallman, and J. Kostamovaara, "An 80x25 pixel CMOS single-photon sensor with flexible on-chip time gating of 40 subarrays for solid-state 3-D range imaging," *IEEE J. Solid-State Circuits*, vol. 54, no. 2, pp. 501–510, Nov. 2018.

[17] D. Bronzi, Y. Zou, F. A. Villa, S. Tisa, A. Tosi, and F. Zappa, "Automotive three-dimensional vision through a single-photon counting SPAD camera," *IEEE Trans. Intell. Transp. Syst.*, vol. 17, no. 3, pp. 782–795, Oct. 2015.

[18] F. Mattioli Della Rocca *et al.*, "A 128 × 128 SPAD motion-triggered time-of-flight image sensor with in-pixel histogram and column-parallel vision processor," *IEEE J. Solid-State Circuits*, vol. 55, no. 7, pp. 1762–1775, Jul. 2020.

[19] A. Ronchini Ximenes, P. Padmanabhan, M. Lee, Y. Yamashita, D. Yaung, and E. Charbon, "A modular, direct time-of-flight depth sensor in 45/65-nm 3-D-Stacked CMOS technology," *IEEE J. Solid-State Circuits*, vol. 54, no. 11, pp. 3203–3214, Nov. 2019.

[20] A. Rochas *et al.*, "Low-noise silicon avalanche photodiodes fabricated in conventional CMOS technologies," *IEEE Trans. Electron. Devices*, vol. 49, no. 3, pp. 387–394, 2002.

[21] L. Pancheri and D. Stoppa, "Low-noise CMOS single-photon avalanche diodes with 32 ns dead time," in *Proc. ESSDERC - 37th Eur. Solid-State Device Res. Conf.*, Munich, Germany, 2007, pp. 362–365.

[22] M. Perenzoni, L. Pancheri, and D. Stoppa, "Compact SPAD-based pixel architectures for time-resolved image sensors," *Sensors*, vol. 16, no. 5, May 2016, Art. no. 745, doi: 10.3390/s16050745.

[23] J. Kostamovaara *et al.*, "On laser ranging based on high-speed/energy laser diode pulses and single-photon detection techniques," *IEEE Photon. J.*, vol. 7, no. 2, Apr. 2015, Art. no. 7800215.

[24] J. Kostamovaara, S. Jahromi, and P. Keränen, "Temporal and spatial focusing in SPAD-based solid-state pulsed time-of-flight laser range imaging," *Sensors*, vol. 20, no. 21, Oct. 2020, Art. no. 5973.

[25] S. Jahromi *et al.*, "A 32 × 128 SPAD-257 TDC receiver IC for pulsed TOF solid-state 3-D imaging," *IEEE J. Solid-State Circuits*, vol. 55, no. 7, pp. 1960–1970, Jul. 2020.

[26] S. Jahromi, J.-P. Jansson, P. Keränen, E. A. Avrutin, B. S. Ryvkin, and J. T. Kostamovaara, "Solid-state block-based pulsed laser illuminator for single-photon avalanche diode detection based time-of-flight 3D range imaging," *Opt. Eng.*, vol. 60, no. 5, May 2021, Art. no. 054105.

[27] C. Niclass *et al.*, "Design and characterization of a 256x64-pixel single-photon imager in CMOS for a MEMS-based laser scanning time-of-flight sensor," *Opt. Exp.*, vol. 20, no. 11, pp. 11863–11881, May 2012.

[28] C. Rogers *et al.*, "A universal 3D imaging sensor on a silicon photonics platform," *Nature*, vol. 590, pp. 256–261 Feb. 2021.

[29] G. Fouche, "Detection and false-alarm probabilities for laser radars that use geiger-mode detectors," *Appl. Opt.*, vol. 42, no. 27, pp. 5388–5398, 2003.

[30] M. Henriksson, "Detection probabilities for photon-counting avalanche photodiodes applied to a laser radar system," *Appl. Opt.*, vol. 44, no. 24, pp. 5140–5147, 2005.

[31] P. Keranen and J. Kostamovaara, "256×8 SPAD array with 256 column TDCs for a line profiling laser radar," *IEEE Trans. Circuits Syst. I Regular Papers*, vol. 66, no. 11, pp. 4122–4133, Nov. 2019.

[32] B. S. Ryvkin, E. A. Avrutin, and J. Kostamovaara, "Asymmetric-waveguide laser diode for high-power optical pulse generation by gain switching," *J. Lightw. Technol.*, vol. 27, no. 12, pp. 2125–2131, Jun. 2009.

[33] J. Huikari, J. Nissinen, B. Ryvkin, E. Avrutin, and J. T. Kostamovaara, "High-energy picosecond pulse generation by gain switching in asymmetric waveguide structure multiple quantum well lasers," *J. Sel. Top. Quantum Electron.*, vol. 21, no. 6, pp. 189–194, Mar. 2015.

[34] L. W. Hallman, J. Huikari, and J. Kostamovaara, "A high-speed/power laser transmitter for single photon imaging applications," *Sensors*, pp. 1157–1160, Dec. 2014, doi: 10.1109/ICSENS.2014.6985213.

[35] D. Bimberg, K. Ketterer, E. H. Bottcher, and E. Scoll, "Gain modulation of unbiased semiconductor lasers: Ultrashort pulse generation," *Int. J. Electron.*, vol. 60, no. 23, pp. 23–45, 1986.

[36] P. Vasil'ev, "Ultrafast diode lasers: Fundamentals and applications. Boston/London," 1995, Artech House, Inc.

[37] S. Pellegrini, G. Buller, J. Smith, A. Wallace, and S. Cova, "Laser-based distance measurement using picosecond resolution time-correlated single-photon counting," *Meas. Sci. Technol.*, vol. 11, pp. 712–716, 2000.

[38] S. Jahromi, J.-P. Jansson, and J. Kostamovaara, "Solid-state 3D imaging using a 1 nJ/100 ps laser diode transmitter and a single photon receiver matrix," *Opt. Exp.*, vol. 24, pp. 21619–21632, Sep. 2016.

[39] C. Zhang *et al.*, "A 240 x 160 3D stacked SPAD dToF image sensor with rolling shutter and in pixel histogram for mobile devices," *IEEE Open J. Solid-State Circuits Soc.*, early access, doi: 10.1109/OJSSCS.2021.3118332.

[40] A. K. Pediredla, "Signal processing based Pile-up compensation for gated single-photon avalanche diodes," 2018, *arXiv:1806.07437*.

[41] P. Keranen and J. Kostamovaara, "256 × 8 SPAD array with 256 column TDCs for a line profiling laser radar," *IEEE Trans. Circuits Syst. I Regular Papers*, vol. 66, no. 11, pp. 4122–4133, Nov. 2019.

[42] U. Kabuk, "4D Solid-State lidar," in *Proc. Int. SPAD Workshop ISSW*, Edinburgh, U.K., 2020, Art. no. 30.

[43] C. Zhang, S. Lindner, I. M. Antolović, J. Mata Pavia, M. Wolf, and E. Charbon, "A 30-frames/s, 252 x 144 SPAD flash LiDAR with 1728 dual-clock 48.8-ps TDCs, and pixel-wise integrated histogramming," *IEEE J. Solid-State Circuits*, vol. 54, no. 4, pp. 1137–1151, Apr. 2019.